# Shear-induced formation of vesicles in membrane phases: Kinetics and size selection mechanisms, elasticity versus surface tension

L. Courbin and P. Panizza*

*Centre de Physique Moléculaire Optique et Hertzienne, UMR 5798, Université Bordeaux I, 351 Cours de la Libération, 33400 Talence, France*

(Received 17 September 2003; published 23 February 2004)

Multilamellar vesicles can be formed upon shearing lamellar phases ($L_\alpha$) and phase-separated lamellar-sponge ($L_\alpha/L_3$) mixtures. In the first case, the vesicle volume fraction is always 100% and the vesicle size is monitored by elasticity (''onion textures''). In the second system the vesicle volume fraction can be tuned from 0 to 100% and the mean size results from a balance between capillary and viscous forces (''Taylor droplets''). However, despite these differences, in both systems we show that the formation of vesicles is a strain-controlled process monitored by a universal primary buckling instability of the lamellae.

DOI: 10.1103/PhysRevE.69.021504 PACS number(s): 83.50.Ax, 66.10.−x, 77.22.Gm

## INTRODUCTION

At high concentrations, surfactant molecules in solution may assemble to form membranes (or bilayers). At thermal equilibrium, their topology is given in a first approximation, neglecting the entropy, by a minimization of the elastic energy: $E=(\kappa/2)\int\int[c_1+c_2]^2dS+\tilde{\kappa}\int\int c_1c_2dS$, where $c_1$ and $c_2$ are the two radii of curvature, and $\kappa$ and $\tilde{\kappa}$ the elastic bending and the Gaussian bending constants, both having units of energy [1, 2]. The first part corresponds to the energy cost to bend a bilayer from its flat configuration. The second part is only a function of the topology of the surface as derived by Gauss and Bonnet [3]: $E_{Gaussian}=\tilde{\kappa}\int\int c_1c_2dS=4\pi\tilde{\kappa}(n-g)$, where $n$ and $g$ are respectively the numbers of independent surfaces and of handles. On these grounds, when $\tilde{\kappa}$ is a negative, spherical geometry (i.e., vesicle) is favored for $\tilde{\kappa}/\kappa<-2$ and the lamellar (or $L_\alpha$) phase for $-2<\tilde{\kappa}/\kappa<0$. When $\tilde{\kappa}$ becomes positive, the formation of handles is promoted, leading to the stability of the sponge (or $L_3$) phase [4]. Since such membrane phases are constituted of surfaces differently stacked in space, strong couplings between flow and their structure can be anticipated. In the past decade, a large experimental effort has been devoted to characterizing these couplings, leading to a non-Newtonian behavior [5]. Without any doubt, the most extraordinary example of such coupling is the formation of a structure made of closed compact multilamellar vesicles (MLVs), obtained upon shearing either $L_\alpha$ phases [6–10] or $L_\alpha/L_3$ two-phase coexisting regions [11,12]. Due to their potential applications [13,14] in pharmacology for drug delivery, in biochemistry catalysis, and in cosmetics, this shear-induced structure, which does not exist at equilibrium, has drawn much interest in the past few years. In this paper, we investigate the mechanisms of the formation and size selection of such structures. In a previous paper [15], we have already reported preliminary results for an inverse lamellar phase made of sodium dodecyl sulfate, water, pentanol, and dodecane. In what follows, however, we consider two different systems, namely, a direct $L_\alpha$ phase and a $L_\alpha/L_3$ phase-separated mixture both made with sodium bis(2-ethylhexyl) sulfosuccinate, and brine. We focus more specifically on conductivity measurements and show that the formation of MLVs results in both systems from a universal *strain controlled* process likely monitored by a buckling instability of the membranes, as inferred from recent theories.

## EXPERIMENTAL SYSTEMS

To investigate the effect of flow on $L_\alpha$ phases, we work both with a direct and an inverse lamellar phase, stabilized by undulation interactions [16]. The first system is a pseudo binary mixture made of 20-wt.% sodium bis(2-ethylhexyl) sulfosuccinate (AOT) and 80-wt.% brine (sodium chloride) whose phase diagram has already been published by Gosh and Miller [17]. In this water system, $\tilde{\kappa}$ is strongly affected by the salinity $S$, which screens the interaction between polar heads. It is negative at low salinities and increases with $S$. On the other hand, $\kappa\approx 3k_BT$ [18] does not depend on $S$. At 25 °C, for low salinities ($S=1.4\%$), the equilibrium phase is a direct lamellar phase ($L_\alpha$) whereas, for high salinities ($S>2\%$), the bilayers interconnect randomly and form a Newtonian bicontinuous phase referred to in Literature as sponge phase (or $L_3$ phase) [4]. For intermediate salinities, a coexistence of these two phases is observed (see Fig. 1).

The second system is made of sodium dodecyl sulfate (SDS), pentanol, dodecane and water. For a *SDS/water* weight ratio of 1.55, the phase diagram of this quaternary system presents a large lamellar region [19]. This lamellar phase is constituted of water films surrounded by surfactant molecules and separated by a solvent which is a mixture of 91-wt.% dodecane and 9-wt.% pentanol. By changing the dilution, the inter-membrane distance can be varied continuously from 40 up to 300 Å. Along this dilution path, the membrane thickness $\delta=2.6$ nm and $\kappa\approx k_BT$ [20] remain fixed. In what follows, we will refer to this inverse lamellar phase as the oil system.

### A. Shear cells

Small angle light scattering (SALS) experiments are performed under shear flow with home-made transparent Cou-

*Email address: p.panizza@cpmoh.u-bordeaux1.fr

 

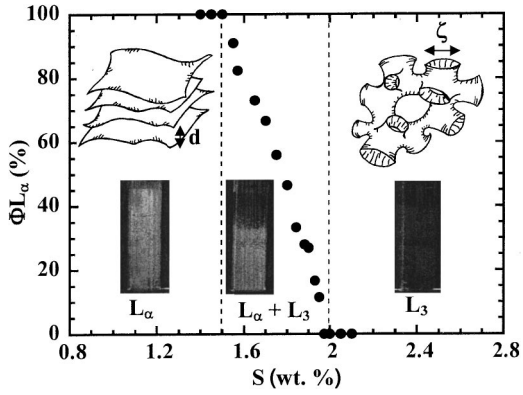


FIG. 1. Phase diagram of a pseudobinary system consisting of 20-wt. % AOT and 80-wt. % brine as a function of $S$, the weight fraction of salinity. The temperature is set to 25 °C. Insets: shown are schematic representations of lamellar (smectic distance $d$) and sponge structures (pore size $\zeta$) and visualizations between crossed polarizers of a test tube containing solutions prepared with different brine weight fractions.

ette cells. The inner cylinder (radius $R_i = 25$ mm) is fixed while the outer one rotates at a constant angular velocity $\omega$. With such a flow geometry, simple Newtonian fluids exhibit a quasiconstant shear rate. However, when the gap is filled with non-Newtonian materials (such as liquid crystals, for instance), the flow may become more complex. Nevertheless, we keep the name shear rate and notation $\dot{\gamma} = R_o\omega/D$, where $D$ is the width of the annular gap between the two coaxial cylinders and $R_o$ the outer radius. This quantity represents the mean shear rate through the gap. By changing the rotor, it is possible to vary $D$ from 500 $\mu$m to 2 mm. For every setup that we use, note that $D$ is much smaller than $R_o$. Consequently, the steady state stress and local shear rate can be considered as nearly uniform in the whole cell [21]. Briefly, a circularly polarized He-Ne laser beam (wavelength is $\lambda = 632.8$ nm in vacuum) passes through the cell along the shear gradient direction ($\vec{\nabla} V$) and probes the sample in only one of the gaps. The scattered pattern corresponding to light scattered in the velocity-vorticity ($\vec{V}, \vec{Z}$) plane is digitalized, by means of a CCD video camera coupled to a personal computer for the frame acquisition and analysis. Two electrodes, mounted on the stator, allow us to measure the conductivity of the sample along the velocity direction [22,23]. Microscopic observations are performed either *in situ* with a commercial Rheovisometer (Rheocontrol, France), using a cone-plate cell or by removing the sample from the cell and observing it between crossed polarizers.

### B. Lamellar phases

#### *1. Steady states*

As previously shown by Diat and co-workers [6,24] and later by others authors [7,9,25–27], above a critical shear rate $\dot{\gamma}_c$ of the order of a few $s^{-1}$, lamellar phases may become unstable under shear flow. The lamellae then roll up to form an assembly made of micrometric closed compact multilamellar vesicles, known in literature as the onion texture.

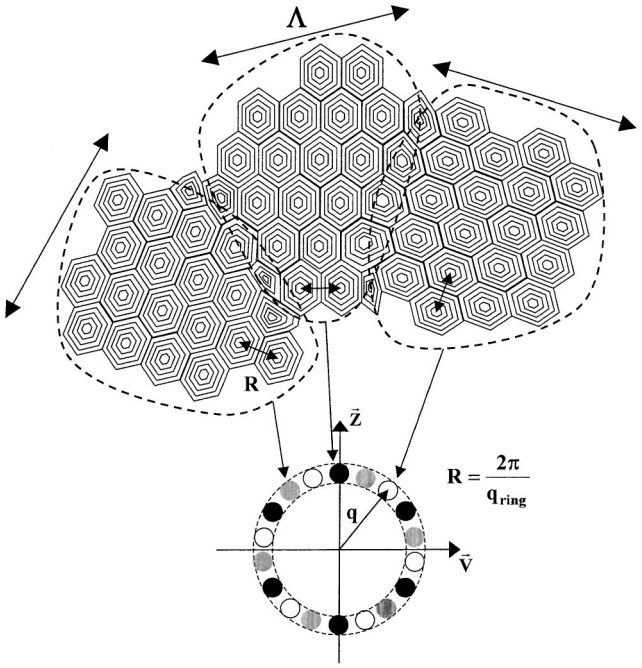


FIG. 2. Shown is a schematic representation of the so-called glassy onion texture adapted from Ref. [29]. Within each monodomain of size $\Lambda$, the vesicles are periodically staked. In SALS, each domain gives rise to six well defined Bragg peaks located at $q = q_{ring} = 2\pi/R$ where $R$ is the distance between adjacent vesicles centers. The random orientation of the monodomains leads in SALS to an isotropic ring.

For a given shear rate $\dot{\gamma} > \dot{\gamma}_c$, the steady state size distribution of the formed vesicles is very narrow, the mean size being controlled by $\dot{\gamma}$.

Prior to the study of the formation kinetics of MLVs, let us first characterize the final steady state onion texture in the water system as a function of $\dot{\gamma}$ and $S$ by means of SALS, optical microscopy, and rheology. In agreement with previous studies [6,7,12], once a constant shear rate $\dot{\gamma} > 1\ s^{-1}$ is applied to this $L_\alpha$ phase, after a transient regime which can be very long, typically a few hours, we witness the emergence of a scattering ring in SALS. This ring clearly shows that a shear-induced micrometric structure has formed in the solution. Optical microscopy observations made between crossed polarizers allow us to identify this structure as an onion texture. The isotropy of this ring indicates that this onion texture has a glassy structure. Indeed, as revealed by cryofracture experiments [28], it consists of an assembly of randomly oriented monodomains of size $\Lambda$ in which the polyhedral closed compact vesicles present a periodical stacking (Fig. 2) [29].

From the position of the scattering ring, $q_{ring}$, the vesicle size can then be measured according to the relation $R = 2\pi/q_{ring}$. It decreases continuously from a few micrometers to a tenth of it upon increasing the value of shear rate (see Fig. 3). For all the solutions prepared, we find that the size $R$ increases strongly with $S$, and scales with $\dot{\gamma}$ according to $R \propto \dot{\gamma}^\alpha$ with $\alpha \approx -0.5$ (see the inset of Fig. 3). The value of this exponent is found on very different systems [12,24,30], and therefore seems to be a universal feature of

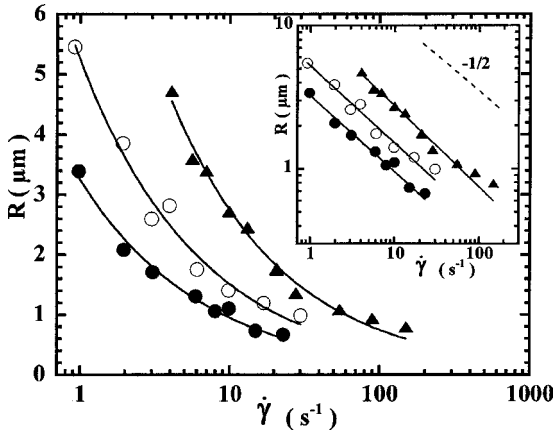


FIG. 3. Variation of the vesicle size $R$ as a function of shear rate $\dot{\gamma}$, derived from SALS measurements. Different symbols correspond respectively to solutions (water system) with $S=1.3\%$ (●), $S=1.4\%$ (○) and $S=1.5\%$ (▲). The lines correspond to the best power law fits $R\propto\dot{\gamma}^{\alpha}$: one finds, respectively, $R=3.25\dot{\gamma}^{-(0.53\pm0.03)}$, $R=5.24\dot{\gamma}^{-(0.54\pm0.03)}$, and $R=10.07\dot{\gamma}^{-(0.55\pm0.02)}$. Inset: log-log plot. The dashed line, a guide for the eyes, has a slope of $-1/2$.

glassy onion textures. According to Diat *et al.* [24], the steady state size $R$ results from a mechanical balance between the viscous stress $4\pi R^2\eta\dot{\gamma}$ and the elastic one $4\pi(2\kappa+\tilde{\kappa})/d$, where $d$ and $\eta$, respectively, stand for the smectic distance and the solution viscosity. This model yields a relation $R\approx\sqrt{(2\kappa+\tilde{\kappa})/(\eta d\dot{\gamma})}$ [Eq. (1)], whose $\dot{\gamma}^{-1/2}$ dependence is in good agreement with experimental observations provided that the solution is Newtonian (i.e., constant viscosity). In order to check this point, we measure with our stress-controlled rheometer, $\eta$, the onion steady state viscosity as a function of $\dot{\gamma}$ (Fig. 4). We find that it varies according to $\eta\propto\dot{\gamma}^{-\nu}$, with $\nu=0.75+0.05$. The same value of this exponent has been obtained by other authors on

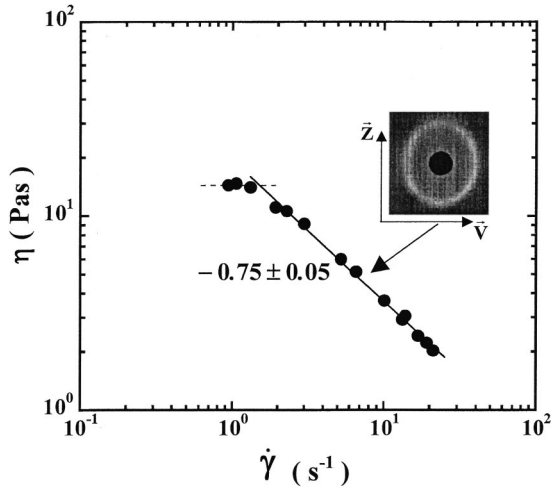


FIG. 4. Variation of $\eta$, the steady state viscosity as a function of $\dot{\gamma}$ for the water system ($S=1.4\%$ and $T=25\,^{\circ}$C). The solid line stands for the best power fit in the MLV region: $\eta=18.33\dot{\gamma}^{-(0.75\pm0.05)}$. Inset: shown is the SALS pattern characteristic of the steady state onion texture.

many different systems [31–33]. It is in good agreement with the value, $\nu=0.8$, predicted by Kleman *et al.* [34], using an analogy with the theory of high temperature creep in metal and alloys [35]. Now, if one inserts this shear-thinning viscosity ($\eta\propto\dot{\gamma}^{-0.75}$) into Eq. (1), a scaling behavior $R\propto\dot{\gamma}^{-0.12}$ not consistent with experimental observations is obtained. However if in Eq. (1) one replaces the viscosity of the solution by that of solvent the correct $\dot{\gamma}^{-1/2}$ experimental dependence is then obtained. Taking $d\approx10^{-8}$ m, $\dot{\gamma}=10$ s$^{-1}$, and $(2\kappa+\tilde{\kappa})\approx k_BT$, and, for $\eta$, the viscosity of the solvent (i.e., $\eta=10^{-3}$ Pas) and replacing them in Eq. (1) gives a theoretical size $R\approx6\,\mu$m, which is of the order of the measured one. Unfortunately in that case, a limitation of the model concerns the variation of $R$ with $d$. Comprehensive experimental work by Diat and Roux shows that $R\propto\dot{\gamma}^{-1/2}d^{-2}$ [24], whereas relation (1) then yields a $d^{-1/2}$ dependence. Despite this limitation, the model however qualitatively accounts for (i) the increase of $R$ with $S$ (see Fig. 3) since the energy cost to roll up a flat bilayer into a spherical vesicle, $E=4\pi(2\kappa+\tilde{\kappa})$, increases when approaching the $L_3$ phase (i.e., when $S$ increases) and (ii) the decrease of $R$ when the solvent viscosity is enhanced. Another attempt to explain the variation of $R$ with $\dot{\gamma}$ has been proposed by Van der Linden *et al.* [37]. Following Taylor's approach used for dilute emulsions [36], these authors suggest instead that $R\approx\sigma_{\mathrm{eff}}/\tau$ where $\sigma_{\mathrm{eff}}=\sqrt{K\bar{B}}$ and $\tau=\eta\dot{\gamma}$, are respectively the pseudosurface tension necessary to deform a multi-lamellar vesicle [38] and the viscous stress. Unfortunately, the variation predicted by their model, namely $R\propto\dot{\gamma}^{-0.25}$, is not consistent with the experimental results obtained at fixed shear rate. As a conclusion, the variation of the MLVs size with shear rate is universal to glassy onion structures and remains so far unexplained.

### *2. Formation*

Let us now focus more specifically on the formation kinetics of MLVs under shear flow. Figure 5(a) shows the evolution of the SALS pattern observed after a constant shear rate, $\dot{\gamma}$, is applied to a $L_{\alpha}$ phase. In agreement with observations made by Zipfel *et al.* [39], on a nonionic lamellar system, for both water and oil systems, we first notice an anisotropic enhancement of the SALS pattern slightly elongated in the vorticity direction [see the insets of Figs. 5(a)–5(d)]. After a well defined time delay, $t_e$, a scattering ring, suddenly appears, at a finite wave-vector $q=q_e$, [insets of Figs. 5(a) and 5(b)]. Then, its position moves continuously towards larger wave-vectors [Fig. 5(b)], until reaching its final position, $q=q_f\propto\dot{\gamma}^{1/2}$, characteristic of the steady state onion structure [see the inset of Fig. 5(c)]. When the flow is stopped before $t_e$, the texture we observe between crossed polarizers is very similar to the one prior to shearing [Fig. 5(a)]. On the other hand, observations made for $t=t_e$ and $t>t_e$ reveal a homogeneous texture which is very similar to that of the final onion steady state [Figs. 5(a)–5(c)]. Our observations made on two different $L_{\alpha}$ phases (water and oil systems) are very different from those made by Léon *et al.* [40] on a very dilute AOT system. Namely, we do never observe the nucleation of any large isolated vesicles which

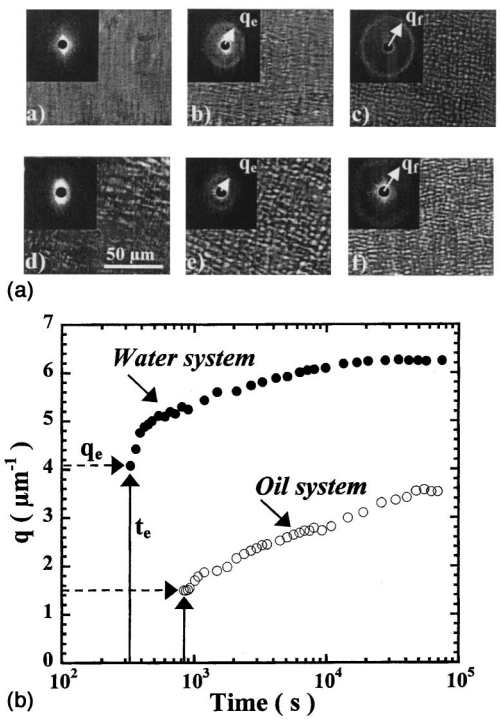


FIG. 5. (a) Optical microscopy images of both water and oil lamellar phases obtained in the rheovisiometer at different times $t$ after a constant shear rate is applied. ($a$) $t=100$ s, ($b$) $t=350$ s, and ($c$) $t=56500$ s correspond to the water system ($\dot{\gamma}=15\ s^{-1}$); figures ($d$) $t=450$ s, ($e$) $t=880$ s and ($f$) $t=69000$ s to the oil system ($\dot{\gamma}=6\ s^{-1}$). Insets: shown are the variations of the SALS pattern during the kinetics. (b) Variation (for both $L_a$ phases) of the position of the Bragg peak $q$ as a function of time, observed in SALS after a constant shear rate is applied: oil system (○) and water system (●). The oil system is made of 15.1-wt. % SDS, 14.55-wt. % pentanol, 47-wt. % dodecane and 23.35-wt. % water ($d=95$ Å) and $\dot{\gamma}=6\ s^{-1}$. The water system is made of 20-wt. % AOT and 80-wt. % brine ($S=1.4\%$). The applied shear rate is $\dot{\gamma}=15\ s^{-1}$.

then align and fill the shearing cell. In agreement with a recent work of Nettensheim *et al.* [41], our observations suggest instead that the shear-induced formation of MLVs does not occur through a nucleation process but more likely through a *hydrodynamic instability* of the membranes, as expected from theories. Let us develop this point into more details. Indeed, a few years ago, inspired by the work of Ostwald *et al.* on smectic A phases [42,43], Diat and Roux have conjectured that the shear-induced transition to MLVs is triggered by a buckling (or undulation) instability [24]. According to them, this instability occurs because the gap spacing is not uniform in the experiment. At rest (i.e., without any shear flow), the existence of dislocations accommodates the spatial variation in the gap cell by permitting a change in the number of layers. At low shear rates, these dislocations can move with the mean flow whereas at higher shear rates they can no longer follow it. This is believed to give rise to an effective dilative strain perpendicular to the layer, leading first to a buckling instability, likely followed by a secondary process leading to onion formation. Along

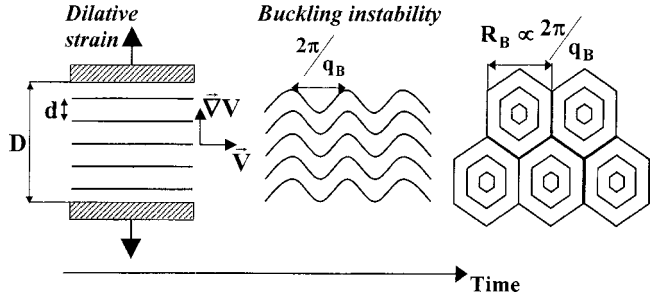


FIG. 6. Shown is a schematic representation of the buckling scenario, adapted from Ref. [45].

these lines, a theory has been put forth with some success by Wunenburger *et al.* [44]. More recently, based on the coupling between the thermal undulations of the membrane and the flow, another buckling scenario, which exists even at uniform gap spacing, has been suggested by Zilman and Granek [45]. According to these authors, the suppression by the flow of the short wavelength membrane undulations generates an effective lateral pressure, leading to a buckling instability similar to that obtained by dilative strain. The instability threshold predicted by this theory is in good agreement with experimental data provided that the viscosity of solvent is replaced by that of the $L_\alpha$ phase. According to these authors, because of its resistance to the flow, the buckling pattern, once it has developed, is believed to become unstable at its turn. The lamellae do then likely roll up to form vesicles (onions) which can flow more easily (Fig. 6). More recently, Marlow and Olmsted [46] suggested that an effective tensionof the membranes may also result from (i) a distortion of the thermal fluctuations under shear flow, (ii) the existence of a frictional force during the dynamical contact between adjacent membranes, or (iii) the transverse force due to collision between membranes. According to them, this effective tension should lead to a decrease of the smectic distance, as observed by Yamamoto and Tanaka [47] on a very dilute lamellar phase. However, when permeation is disallowed or too slow, the system cannot any longer reduce $d$. It is therefore submitted to a dilative strain perpendicular to the plane of membranes which, above a critical shear rate, can induce a buckling instability. Although the origin of the effective tension is still under debate, so far all theoretical models agree that the MLV formation results from a primary buckling instability of the lamellae and requires the existence of dislocations.

To get more information on the buckling mechanism, we first study $q_e$ as a function of $\dot{\gamma}$ (Fig. 7). For both water and oil lamellar systems, we get $q_e \propto \dot{\gamma}^{1/3}$, a result similar to the prediction derived by Zilman and Granek (ZG) for $q_B$, the most unstable wave vector of the buckling instability [45], namely, $q_B \approx 2.6(\eta d/\kappa D)^{1/3}\dot{\gamma}^{1/3}$ [Eq. (2)]. To further check this point, we also perform a systematic study of $q_e$ as a function of $D$ and $d$ in the oil system (Fig. 8). The result we obtain: $q_e = s(d/D)^{1/3}\dot{\gamma}^{1/3}$ (where $s \approx 50\ \mu m^{-1}\, s^{1/3}$), is still consistent with the expression found by ZG for $q_B$. However a good numerical agreement between theoretical prediction and experimental data [i.e., $s \approx 2.6(\eta/\kappa)^{1/3}$] requires in both water ($s \approx 87\ \mu m^{-1}\, s^{1/3}$) and oil systems (Fig. 9) to take for the viscosity $\eta$ in Eq. (2) values of the order of 10–100 Pas,

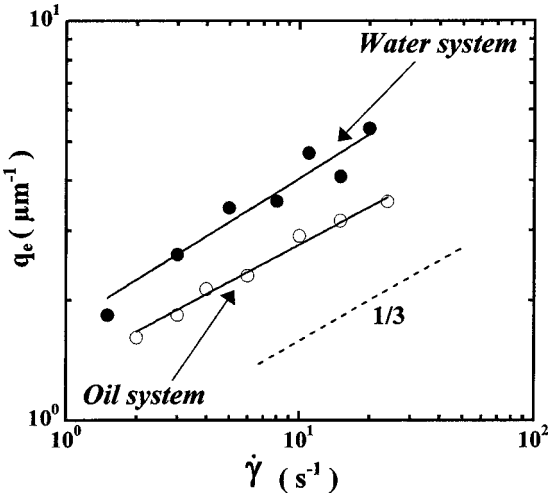


FIG. 7. Variation of $q_e$ as a function of $\dot{\gamma}$ for both the water system (●) and the oil system (○). The oil system consists of 10.62-wt. % SDS, 12.91-wt. % pentanol, 60-wt. % dodecane and 16.47-wt. % water ($d=159$ Å). The water system is made of 20-wt. % AOT and 80-wt. % brine ($S=1.4\%$). The solid lines correspond to the best power law fits: $q_e=1.34\dot{\gamma}^{(0.31\pm0.02)}$ for the oil system and $q_e=1.75\dot{\gamma}^{(0.36\pm0.05)}$ for the water one. The dashed line has a slope 1/3 and is a guide for the eyes.

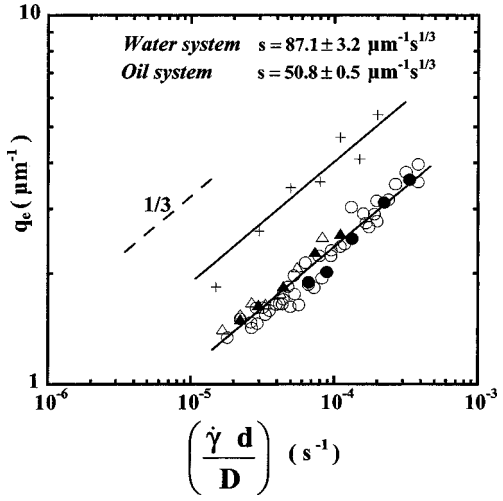


FIG. 9. For both systems, $q_e$ is shown represented on a log-log plot as a function of $(d\dot{\gamma}/D)$ for different values of $d$ and $D$. For the oil system: (○) $D=1$ mm and the different values of $d$ are 73, 83, 89, 95, 111, 131, and 159 Å, (●) $D=0.5$ mm and $d=111$ Å, (▲) $D=1.5$ mm and $d=111$ Å, and (△) $D=2$ mm and $d=111$ Å. For the water system (+), values are: $D=1$ mm and $S=1.4\%$. The best power law fits are respectively: $q_e=(50.8\pm0.5)\times(\dot{\gamma}d/D)^{1/3}$ for the oil system and $q_e=(87.1\pm3.2)(\dot{\gamma}d/D)^{1/3}$ for the water system.

quite higher than that of the solvent. Similar numerical discrepancies arise in most of the theories previously described. Note that this may likely be related to the existence of dislocations in the sample.

Our observations show that the emergence of MLVs results from a *strain-controlled process*, since $t_e\propto\dot{\gamma}^{-\beta}$ with $\beta\approx1$ (Fig. 10). In order confirm this point, we also performed a conductivity measurement along the velocity direction. Figure 11 shows the variation of the conductivity measured along the $\vec{V}$ direction after different constant shear rates are applied to a lamellar phase (oil system) initially at rest. Note that conductivity is valuable information since it is related to the defects and the orientations of the membranes with respect to the flow direction [48]. However, modeling its transient variations is very challenging. Nevertheless, if as the $X$ axis one plots the strain instead of the time, all curves fall on a master curve (see the inset of Fig. 11). Therefore, the strain is clearly the key parameter to understand the formation of MLVs under constant shear rate. For both systems, the critical strain $\gamma_e=t_e\dot{\gamma}$ required to form MLVs is very

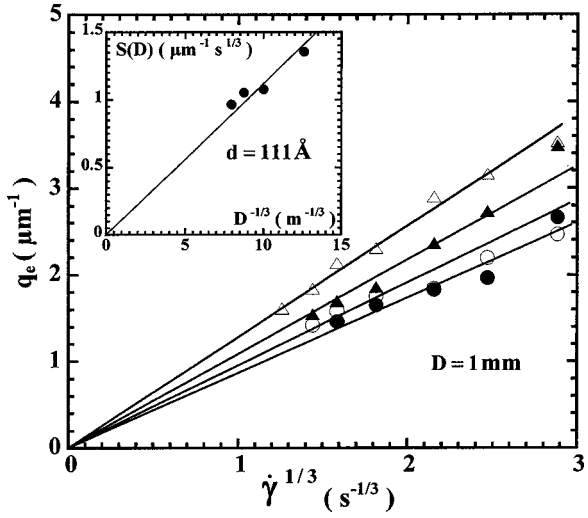


FIG. 8. Shown is $q_e$ as a function of $\dot{\gamma}^{1/3}$ for $D=1$ mm and different values of $d$: (●) $d=73$ Å, (○) $d=89$ Å, (▲) $d=111$ Å, and (△) $d=159$ Å. Inset: shown is the slope $S(D)$ vs $D^{-1/3}$ for $d=111$ Å and different values of $D$. This slope corresponds to the best linear fit: $q_e=S(D)\dot{\gamma}^{1/3}$. The continuous line corresponds to the best linear fit: $S(D)=(0.112\pm0.004)D^{-1/3}$.

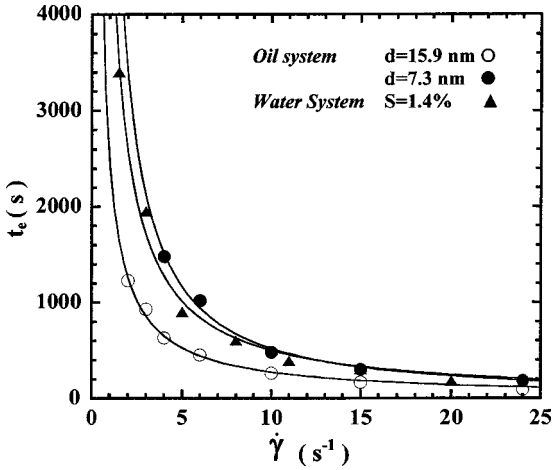


FIG. 10. Variation of $t_e$ as a function $\dot{\gamma}$. For both systems the gap spacing is $D=1$ mm. The lines correspond to the best power law fit: $t_e\propto\dot{\gamma}^{-\beta}$. For the oil system, one finds. $t_e=(2452\pm140.1)\dot{\gamma}^{-(0.96\pm0.05)}$ for $d=159$ Å (○) and $t_e=(7617.8\pm710.2)\dot{\gamma}^{-(1.16\pm0.08)}$ for $d=73$ Å (●). For the water system: $t_e=(5244.6\pm140.1)\dot{\gamma}^{-(1.02\pm0.06)}$ for $S=1.4\%$ (▲).

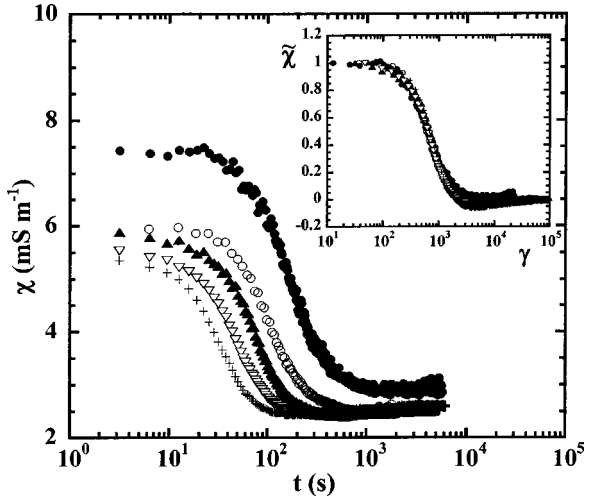


FIG. 11. Variation of the conductivity $\chi$ measured along the $\vec{V}$ direction after a constant shear rate is applied at $t=0$ s to a $L_\alpha$ phase whose composition is 14.05-wt. % SDS, 14.17-wt. % pentanol, 50-wt. % dodecane, and 21.78-wt. % water ($d=111$ Å). The different values of applied shear rates are $\dot{\gamma}=4\ s^{-1}$ (●), $\dot{\gamma}=6\ s^{-1}$ (○), $\dot{\gamma}=10\ s^{-1}$ (▲), $\dot{\gamma}=15\ s^{-1}$ (▽), and $\dot{\gamma}=24\ s^{-1}$ (+). Inset: master curve, shown is the renormalized conductivity defined as $\tilde{\chi}=[[\chi(t)-\chi(\infty)]/[\chi(0)-\chi(\infty)]]$ vs the strain $\gamma=\dot{\gamma}t$.

large, typically a few thousand. A systematic study of $\gamma_e$, made on the oil system, shows that it does not depend on $D$, the gap cell (Fig. 12), and varies roughly as the inverse of the smectic distance $d$ (see the inset of Fig. 13). This variation suggests that $\gamma_e=L/d$, where $L$ is a characteristic distance of the experiment of the order of a few tens of micrometers. This order of magnitude is typically what is expected for a small eccentricity of the Couette cell because of mechanical construction or for the roughness of the walls. An important question can be raised: Is the *strain* or the *number of rotations* the important parameter? To try to elucidate this point, we perform the same experiment with two different cells having the same gap $D=1$ mm but different values of the rotor radius ($R_O^I=16$ mm and $R_O^{II}=26$ mm). For both cells, built with similar conditions, the value of the *critical strain* necessary to form vesicles is identical, whereas the number of rotations differs (Fig. 14).

Therefore the formation of MLVs in $L_\alpha$ phases stabilized by undulation interactions results from a *strain-controlled*

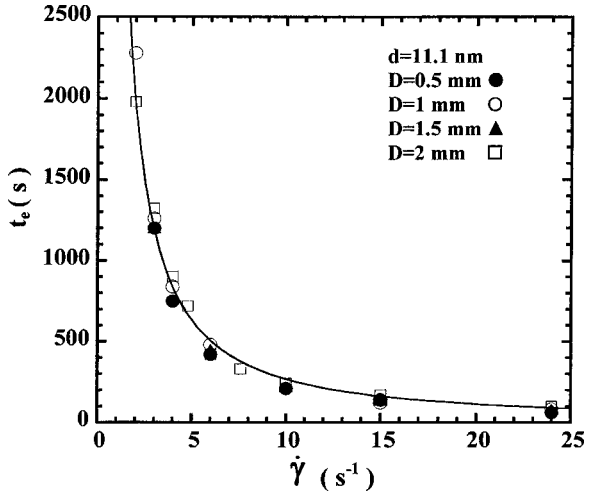


FIG. 12. Shown is $t_e$ as a function of $\dot{\gamma}$ for an oil lamellar phase with $d=111$ Å and different values of the gap spacing: $D=0.5$ mm (●), $D=1$ mm (○), $D=1.5$ mm (▲), and $D=2$ mm (□). The line which corresponds to the best power law fit (for $D=2$ mm): $t_e \propto \dot{\gamma}^{-\beta}$ is $t_e=(4807.1\pm 296.7)\,\dot{\gamma}^{-(1.24\pm 0.06)}$.

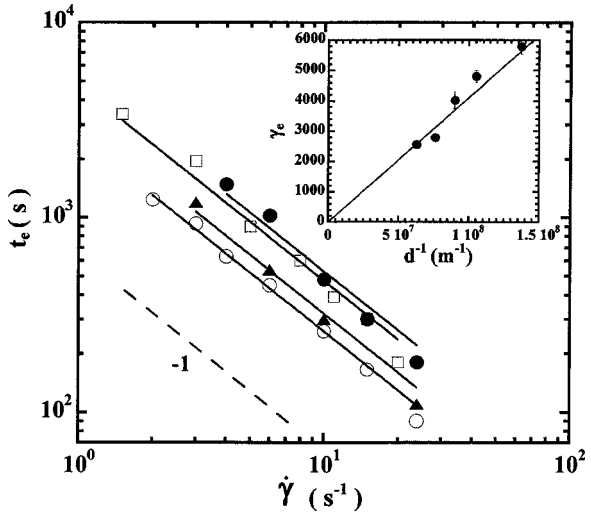


FIG. 13. Shown is $t_e$ vs $\dot{\gamma}$ (oil system) for different values of $d$ and for $D=1$ mm. The solid lines stand for the best fit: $t_e=\gamma_e/\dot{\gamma}$. One finds for the oil system, respectively, $t_e=(5781.6\pm 242.4)/\dot{\gamma}$ for $d=73$ Å (J), $t_e=(3482.7\pm 122.1)/\dot{\gamma}$ for $d=83$ Å (▲), and $t_e=(2562.7\pm 57.7)/\dot{\gamma}$ for $d=159$ Å (○). For the water system ($S=1.4$ wt. %), $t_e=(5166.3\pm 153.2)/\dot{\gamma}$. Inset: shown is the variation of the strain $\gamma_e$ with the smectic distance $d$: $\gamma_e=L/d=(41.1\pm 0.7)\ \mu$m$/d$.

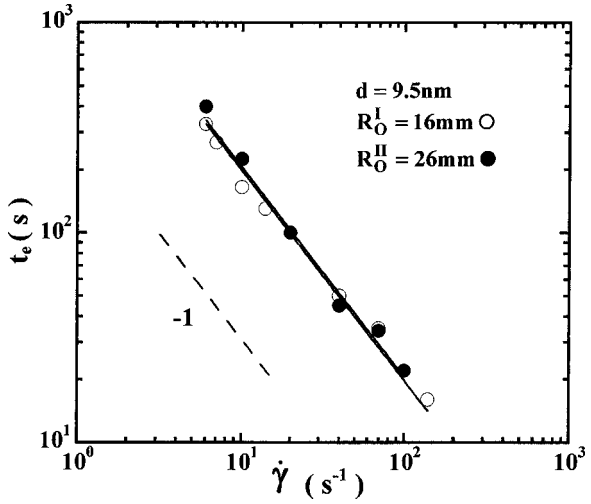


FIG. 14. Shown is $t_e$ vs $\dot{\gamma}$ for different values of $R_o$, the rotor radius, and $D=1$ mm. The lamellar phase consists of 15.1-wt. % SDS, 14.55-wt. % pentanol, 47-wt. % dodecane, and 23.35-wt. % water ($d=95$ Å). Solids lines correspond to the best powerlaw fit $t_e=\gamma_e/\dot{\gamma}$: $t_e=(1976\pm 107)/\dot{\gamma}$ for $R_O^I=16$ mm (○), and $t_e=(2057\pm 138)/\dot{\gamma}$ for $R_O^{II}=26$ mm (●). The dashed line has a slope $-1$ and is a guide for the eyes.

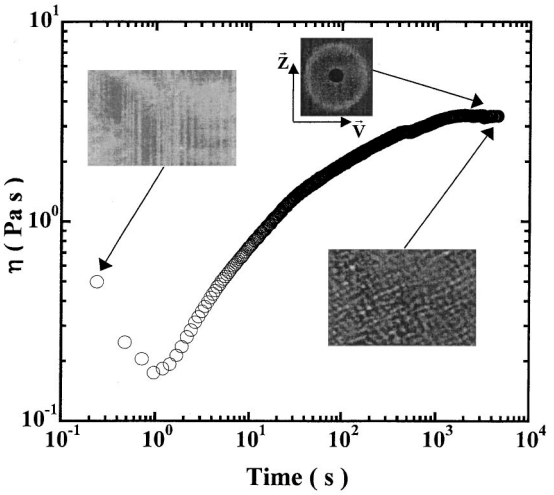


FIG. 15. Variation of the viscosity as a function of time after a constant stress $\sigma=27$ Pa is applied to a $L_\alpha/L_3$ phase-separated solution made of 20-wt. % AOT and 80-wt. % brine ($S=1.6\%$). Insets: Shown are microscope images between crossed polarizers of the premixed $L_\alpha/L_3$ mixture and of the final steady state shear-induced structure. The ring obtained in SALS in the $(\vec{V},\vec{Z})$ direction corresponds to this final state.

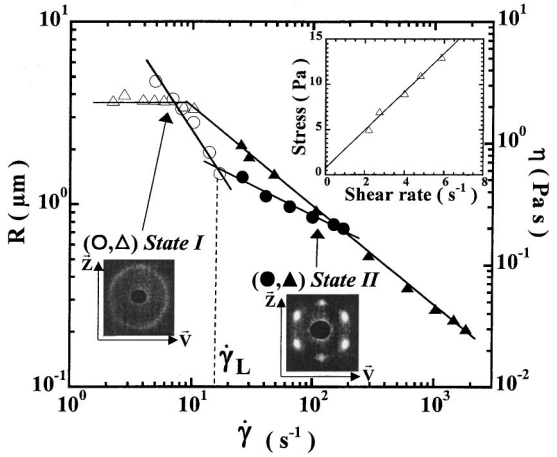


FIG. 16. Variation of the viscosity $\eta$ [(△) and (▲)] and of the steady state droplet size $R$ [(○) and (●)] as a function of $\dot{\gamma}$. The solution is identical to that of Fig. 15. Rheology and SALS measurements are performed on two different Couette cells. As a result, one can notice that the transition between steady states I and II occurs at slightly different values of $\dot{\gamma}_L$. Shown are the SALS patterns observed in the $(\vec{V},\vec{Z})$ plane, in state I [(△) and (○)] and state II [(▲) and (●)]. Inset: stress versus shear rate for small values of shear rates in steady state I. The solid line stands for the best linear fit given by: $\tau=\tau_y+\eta_I\dot{\gamma}$ with $\tau_y=0.7$ Pa and $\eta_I=2.11$ Pa s.

process occurring homogeneously in the cell at a well-defined wave vector $q_e$. A systematic study of $q_e$ as a function of $\dot{\gamma}$, $d$, and $D$ suggests that the formation of MLVs results from a primary buckling instability, as expected from theories.

### C. Lamellar and sponge phase coexisting region

Multilamellar vesicles can also be obtained by subjecting a solution prepared in the $L_\alpha/L_3$ two-phase region [11,12] to shear flow. In order to do so, we prepare solutions in this two-phase region with 20-wt. % AOT and 80-wt. % brine with different salt content ($1.5\% \leqslant S \leqslant 1.7\%$). After a few weeks left at rest, a macroscopic interface between $L_\alpha/L_3$ phases is observed. From the position of this interface, we can estimate $\phi_{L_\alpha}$, the volume fraction of the $L_\alpha$ phase. To investigate the effect of shear flow on this phase-separated system, we first stir it gently in order to obtain a macroscopic homogenous mixture and then pour this mixture into the Couette cell. After shearing it for a few minutes at constant stress, a scattering ring appears on the screen (Fig. 15). Its radius evolves continuously until its reaches its steady state value. If the shear flow is then stopped, the ring persists with the same size, indicating that the shear-induced structure is metastable. When observed under crossed polarizers, the texture is very similar to the so-called onion textures obtained upon shearing $L_\alpha$ phases: it also consists of closed compact monodisperse multilamellar vesicles. Such a texture which has been observed in another $L_\alpha/L_3$ two-phase mixture is consistent with multilamellar droplets immersed into the $L_3$ matrix [11]. A confirmation to this assertion requires SAXS or SANS experiments under shear flow since it is well known that a sponge to lamellar shear-induced transition may occur under flow [49]. Because of the very low electronic contrast between AOT and water and the strong diffusion of the cell at small $q$, SAXS experiments under shear flow are difficult to perform on this system. However, preliminary SANS experiments show that such a shear-induced transition does not occur in similar $L_\alpha/L_3$ two-phase mixtures when water is replaced by $D_2O$ [50]. Therefore, $\phi$, their volume fraction, is not 100% given as for onion textures, but is given by $\phi=\phi_{L_\alpha}$ where $\phi_{L_\alpha}$ is the volume fraction of the $L_\alpha$ phase in the mixture. As a result, the characteristic distance $\xi=2\pi/q_{ring}$ determined by SALS measurements, which indeed corresponds to the distance between two adjacent droplets, is no longer the size $R$ of the droplets, as for the onion texture. Nevertheless, when $\phi=\phi_{L_\alpha}>0.63$, the droplets must deform and therefore become polyhedrons. Neglecting Plateau's borders, taking cubic droplets for simplicity's sake, and assuming that the entire $L_\alpha$ phase is converted into droplets, leads to $\phi \approx (R/\xi)^3$ and therefore to $R \approx \xi\phi^{1/3}$ [12]. Since $\phi>0.63$, $R \approx \xi$, as a consequence a variation of $R$ with $\dot{\gamma}$ can directly be inferred from the SALS measurement of $\xi$. Experimentally, when $\dot{\gamma}$ increases, the final ring becomes larger, indicating that the steady state size of the multilamellar droplets decreases. However, contrary to the onion textures obtained upon shearing $L_\alpha$ phases, $R$ scales herein as $\dot{\gamma}^{-1}$ and not as $\dot{\gamma}^{-1/2}$ (see Figs. 16 and 17). Therefore, the physical mechanism fixing the steady state droplet size differs from that of glassy onion textures. To understand such a discrepancy, more insights can be obtained by noticing that contrary to onion textures, the structure is not shear thinning but instead quasi-Newtonian (Fig. 16). Such a rheological behavior is quite surprising if one considers that the droplet volume frac-

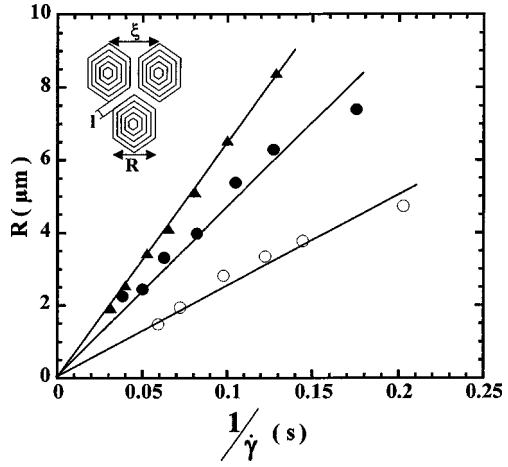


FIG. 17. Variation of the droplet size $R$ in the glassy state (state I) as a function of the inverse applied shear rate $\dot{\gamma}$. The system consists of 20-wt. % AOT and 80-wt. % brine and different values of $S$. Data are obtained from SALS measurements. Solid lines stand for the best linear fit: $R \propto 1/\dot{\gamma}$. The different symbols correspond respectively to $S=1.55\%$ (○) with $R=(25.3\pm0.9)/\dot{\gamma}$, $S=1.6\%$ (●) with $R=(46.9\pm1.8)/\dot{\gamma}$ and $S=1.63\%$ (▲) with $R=(64.6\pm0.5)/\dot{\gamma}$.

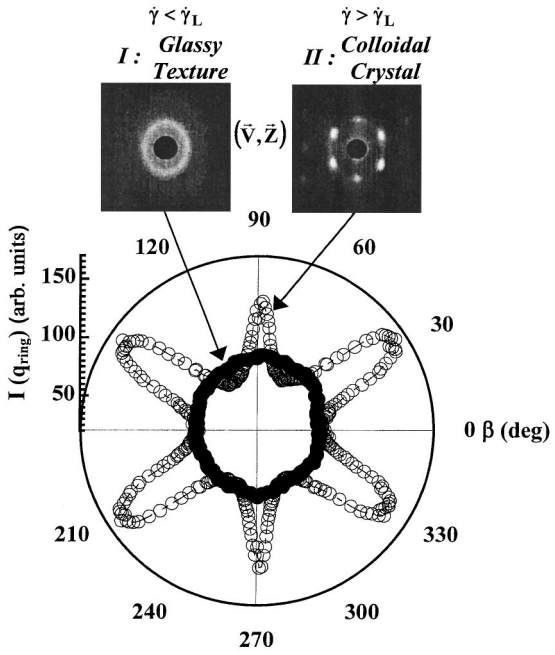


FIG. 18. Shown are the SALS patterns and the angular variations of the Bragg intensities corresponding respectively to the glassy (I, $\dot{\gamma}<\dot{\gamma}_L$) and crystal (II, $\dot{\gamma}>\dot{\gamma}_L$) steady states. In this angular representation, the glassy state is characterized by a ring, while the six Bragg peaks correspond to the colloidal crystal state. Note the loss of intensity of the two peaks in the $\vec{Z}$ direction ($\beta=90°$, $\beta=270°$).

tion is beyond close packing. However, the existence of a yield stress cannot be completely ruled out, since we have not investigated the rheological behavior at very low shear rates. Nevertheless our data extrapolate at a zero shear rate, indicating that the value of this yield stress $\tau_y$ is small compared to the values of applied stresses (i.e., $\tau \approx \eta\dot{\gamma}$) (see the inset of Fig. 16), probably because of the very low value of surface tension between $L_\alpha$ and $L_3$ phases. Combining SALS and rheology measurements shows that the droplet size results from a mechanical balance between viscous stress $\eta\dot{\gamma}$ and Laplace pressure $\sigma/R$ yielding to the well known relation first derived by Taylor in the case of dilute emulsions [36]: $R=\sigma/\tau=\sigma/\eta\dot{\gamma}$ [Eq. (3)] (Fig. 17). Now replacing the value of the measured viscosity in this relation, leads to an estimation for $\sigma$, the surface tension, of the order of $10^{-5}$ $\mathrm{Nm}^{-1}$. This value is in very good agreement with expectation from a crude dimensional analysis: $\sigma \approx k_B T/d^2$, and also with measurements by others authors [51,52]. In this regime, it confirms that the steady droplet size is then monitored by the surface tension between both coexisting phases and not by the elasticity of the lamellar phase. Indeed, this result is not very surprising, if one compares the elastic energy cost to form a multilamellar droplet $E_{elas}=4\pi(\kappa+2\tilde{\kappa})R/d$ to the energy cost $E_{surf}=4\pi R^2\sigma$ to deform it. Above a critical size $R^* \approx (\kappa+2\tilde{\kappa})/(d\sigma)$ [Eq. (4)], the surface tension should overcome the elastic energy cost and therefore competes directly with the viscous stress. To confirm this point, we can compare $R^*$ with the measured droplet sizes. Taking the elastic modulii of the order of $k_B T$, $d \approx 10$ nm and $\sigma \approx 10^{-5}$ $\mathrm{Nm}^{-1}$ leads to a value $R^* \approx 0.1$ $\mu$m much smaller than the micrometric sizes, we measure by SALS.

Let us now go back to the experiments. Very surprisingly, above a critical shear rate $\dot{\gamma}_L \approx 20$ $\mathrm{s}^{-1}$, a splitting of the scattering ring into six well-defined peaks occurs, indicating that a long range order of the droplets with six fold symmetry takes place (Figs. 16 and 18). This effect is similar to the shear-induced ordering, known as the *layering effect*, observed in colloidal suspensions of hard spheres [53], and more recently in some $L_\alpha$ phases [54,55]. It shows that, in the $(\vec{V},\vec{Z})$ planes, the closed compact droplets organize on a triangular lattice and consequently present a hexagonal shape [54]. Under flow, the two Bragg peaks along the $\vec{Z}$ axis appear much less defined than the four other ones (see Fig. 18). This loss of correlation in the $\vec{Z}$ direction can be attributed to a zigzag motion between sliding adjacent planes [53]. In this regime, the droplet size and the viscosity vary respectively as $R \propto \dot{\gamma}^{-1/3}$ and $\eta \propto \dot{\gamma}^{-0.85}$ [Figs. 16 and 19(a)]. The variation of $R$ versus $\dot{\gamma}$ seem universal to the shear-induced colloidal ordering of soft monodisperse multi-lamellar droplets since it is also observed in some $L_\alpha$ phases [55]. As shown in Figs. 19(a) and 19(b), the value of $\dot{\gamma}_L$ characterizing the *disorder/order* transition strongly depends on the salinity. The physical origin of this transition is so far unexplained in both systems. However, it is interesting to note that it occurs in our two-phase system when the film thickness $l \approx \xi - R \approx R(1-\phi^{1/3})/\phi^{1/3}$ between adjacent droplets becomes of the order of a few hundred Å, a length typically of the order of a few times the pore size $\zeta$ of the $L_3$ phase. This fact strongly suggests that this transition may be triggered by a confinement of the interstitial $L_3$ phase. Finally, let us comment on the origin of the very narrow size distribution of droplets in our system. Following Mason and Bibette is discussion for

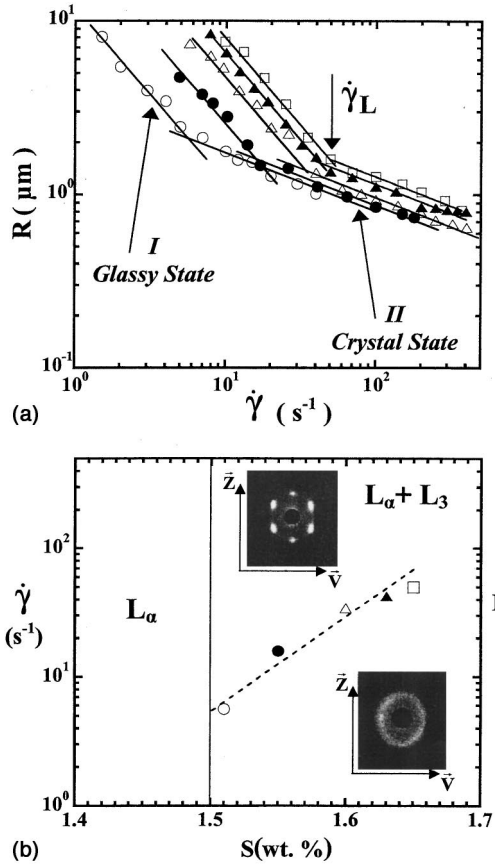


FIG. 19. (a) Log-log plot of the droplet size $R$ versus $\dot{\gamma}$ (SALS measurements), for different values of S. The system consists of 20-wt. % AOT and 80-wt. % brine. Different symbols correspond to $S=1.51\%$ (○), $S=1.55\%$ (●), $S=1.6\%$ (△), $S=1.63\%$ (▲), and $S=1.65\%$ (□). Solid lines correspond to the best power law fits respectively for state I and state II: $R=A_I\dot{\gamma}^{-1}$ and $R=A_{II}\dot{\gamma}^{-1/3}$. $A_I$ and $A_{II}$ units are respectively $\mu\mathrm{m\,s^{-1}}$ and $\mu\mathrm{m\,s^{-1/3}}$. One finds: $A_I=(11.8\pm0.4)$ and $A_{II}=(3.74\pm0.08)$ for $S=1.51\%$, $A_I=(25.3\pm0.9)$, and $A_{II}=(4.01\pm0.07)$ for $S=1.55\%$, $A_I=(46.9\pm1.8)$, and $A_{II}=(4.45\pm0.06)$ for $S=1.6\%$, $A_I=(64.6\pm0.5)$, and $A_{II}=(5.31\pm0.09)$ for $S=1.63\%$ and $A_I=(79.3\pm2.8)$ and $A_{II}=(5.86\pm0.09)$ for $S=1.65\%$. (b) Orientation diagram as a function of $S$ and $\dot{\gamma}$ ($T=25\,^\circ$C). The values of $\dot{\gamma}_L$ are determined from SALS measurements as shown in (a). Symbols are identical to those in (a). The dashed line is a guide for the eyes.

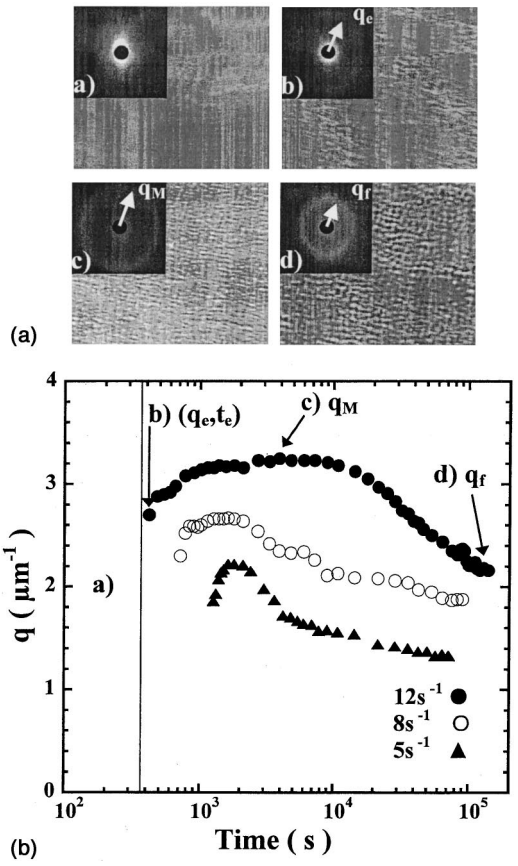


FIG. 20. (a) Evolution of the texture observed between crossed polarizer under microscope prior shearing ($t=0$ s) and after a constant shear rate $\dot{\gamma}=12\ \mathrm{s^{-1}}$ is applied to a premixed $L_\alpha/L_3$ two-phase coexisting mixture for which $S=1.6\%$. Insets: shown are the corresponding SALS patterns observed in the $(\vec{V},\vec{Z})$ plane: (*a*) $t=90$ s, (*b*) $t=t_e=450$ s, (*c*) $t=3900$ s, and (*d*) $t=115200$ s. (b) Temporal variation of the position of the ring $q$ obtained after applying to the premixed $L_\alpha/L_3$ mixture different values of $\dot{\gamma}$: $\dot{\gamma}=5\ \mathrm{s^{-1}}$ (▲), $\dot{\gamma}=8\ \mathrm{s^{-1}}$ (○), and $\dot{\gamma}=12\ \mathrm{s^{-1}}$ (●). The system is identical to (a) and the origin of time is taken when the shear flow is applied.

emulsion [56], let us compare the cell gap spacing, $D$ to a typical fracture plane thickness, $\ell_F$. Assuming that our closed compact droplet system resists flow elastically until the applied stress overcomes $\tau_y$ and flows within a fracture plane of thickness $\ell_F$ which develops between un-yielded sections of the material yields: $\ell_F \approx D\,\eta\dot{\gamma}/\tau_y$ [Eq. (5)]. Since for the range of applied shear rates, $\tau_y \ll \eta\dot{\gamma}$, Equation (5) leads to $\ell_F \gg D$ and therefore to a homogeneous flow in the gap cell. Consequently all droplets are sheared and ruptured at the same shear rate.

### *Formation mechanism*

To elucidate the mechanism of formation of multilamellar droplets in $L_\alpha/L_3$ phase-separated mixtures, we have studied the kinetics of droplet formation by means of SALS and optical microscopy. Figures 20(a) and 20(b) show the evolution of the SALS pattern after a constant shear flow has been applied premixed mixture. As for $L_\alpha$ systems (see Sec. A 1) we first observe a strong anisotropic enhancement of the scattered intensity at small angles [see Fig. 20(a)]. Then, after a time delay $t_e$, a scattering ring suddenly emerges at $q=q_e$ [Figs. 20(a) and 20(b)], and persists with same radius for a few hours when the shear flow is stopped. If a few drops of the sample are then removed from the cell and placed between crossed polarizers under optical microscope, a homogeneous modulation of the optical index [Figs. 20(a) and 20(b)], similar to the texture of closed compact multilamellar droplets can be observed. The variations of the emerging size, $R_e=2\pi/q_e$, and of the delay time, $t_e$, with $\dot{\gamma}$ are identical to what we observe for the $L_\alpha$ system (Fig. 21), namely, $t_e \propto 1/\dot{\gamma}$ and $R_e \propto \dot{\gamma}^{-1/3}$. These results show that the *strain-controlled* process at the origin of the formation of

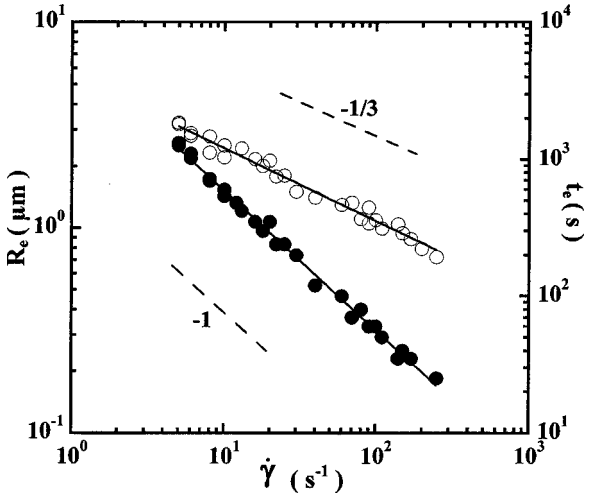


FIG. 21. Variations of the emergence size $R_e = 2\pi/q_e$ and of the delay time $t_e$ defined in Fig. 20(b) as a function of $\dot{\gamma}$. The system is a premixed $L_\alpha/L_3$ mixture ($S = 1.6\%$). Solid lines correspond to the best power law fits: $R_e = (5.52 \pm 0.19)\dot{\gamma}^{-(0.35\pm0.01)}$ and $t_e = (6150 \pm 380)\dot{\gamma}^{-(1.02\pm0.02)}$.

MLVs in $L_\alpha$ phases, likely takes place in the lamellar domains of the $L_\alpha/L_3$ two-phase mixture upon shearing.

As for the $L_\alpha$ system, the initial radius of the MLVs in the $L_\alpha$ domains of the $L_\alpha/L_3$ mixture, $R_e$, does not satisfy a mechanical balance. Therefore, when the shear flow is pursued at $\dot{\gamma}$, the size of the droplets changes continuously in order to reach mechanical equilibrium. However, contrary to $L_\alpha$ systems, this process presents two steps [see Fig. 20(b)]: first, the wave vector $q$ characterizing the scattering ring increases to a pseudo-steady-state value $q_M$ and then it decreases until it reaches its final size, $q_f$. Therefore, the corresponding droplet size $R$, first, decreases to reach a minimum value $R_M = 2\pi/q_M$ and then increases to its equilibrium value $R_f = 2\pi/q_f$. This final size $R_f$ varies as previously said as $\dot{\gamma}^{-1}$, below $\dot{\gamma}_L$, and as $\dot{\gamma}^{-1/3}$ above, while the size $R_M$ scales as $\dot{\gamma}^{-1/2}$ below $\dot{\gamma}_L$, and more as $\dot{\gamma}^{-1/3}$ above (see Figs. 22 and 23). For $\dot{\gamma} \leqslant \dot{\gamma}_L$, the variation of $R_M$ with $\dot{\gamma}$ is identical to the scaling observed for the steady state onion textures obtained upon shearing the $L_\alpha$ phases. This result suggests that once the initial MLVs are formed in the $L_\alpha$

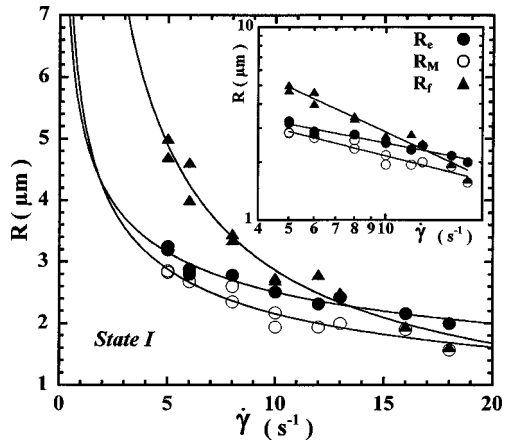


FIG. 22. Variation for state I of the initial $[R_e$ (●)], minimum $[R_M$ (○)], and final droplet sizes $[R_f$ (▲)] defined in Fig. 20(b) as a function of $\dot{\gamma}$. The system is a premixed $L_\alpha/L_3$ mixture ($S = 1.6\%$). The continuous lines correspond to the best power law fits: $R_e = (5.33 \pm 0.31)\dot{\gamma}^{-(0.33\pm0.03)}$, $R_M = (5.64 \pm 0.44)\dot{\gamma}^{-(0.42\pm0.04)}$, and $R_f = (16.95 \pm 1.66)\dot{\gamma}^{-(0.78\pm0.05)}$. Inset: shown are log-log plots.

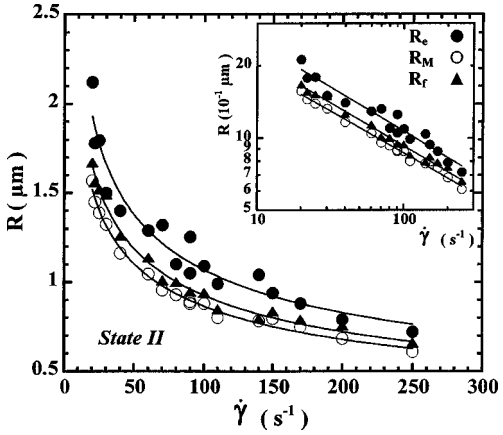


FIG. 23. Variation for state II of the initial $[R_e$ (●)], minimum $[R_M$ (○)], and final droplet sizes $[R_f$ (▲)] defined in Fig. 20(b) as a function of $\dot{\gamma}$. The system is identical to that of Fig. 22. The continuous lines stand for the best power law fits: $R_e = (5.79 \pm 0.53)\dot{\gamma}^{-(0.36\pm0.02)}$, $R_M = (4.34 \pm 0.14)\dot{\gamma}^{-(0.35\pm0.01)}$, and $R_f = (4.85 \pm 0.18)\dot{\gamma}^{-(0.36\pm0.01)}$. Inset: shown are log-log plots.

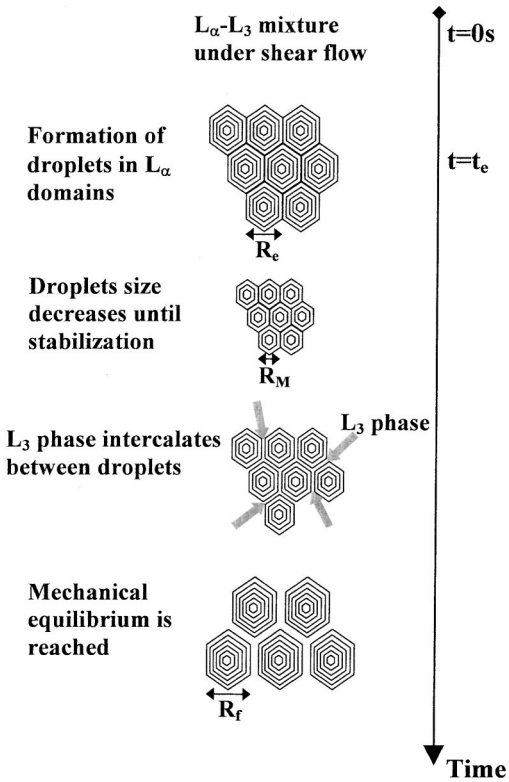


FIG. 24. Schematic representation of the mechanism of droplet formation in $L_\alpha/L_3$ two phase-separated mixtures submitted to a constant shear flow.

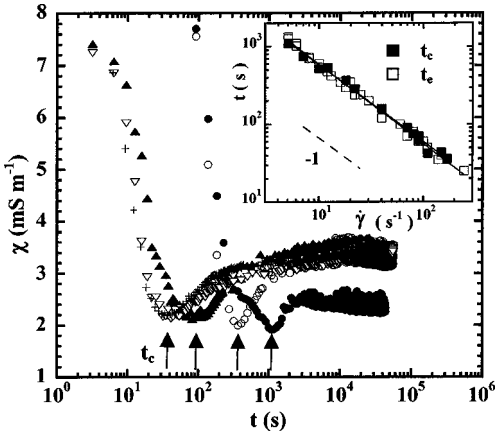


FIG. 25. Variation of the conductivity $\chi$ measured along the $\vec{V}$ direction after a constant shear rate is applied at $t=0$ s to a water system ($S=1.6\%$). The different values of applied shear rates are respectively: $\dot{\gamma}=5\ \mathrm{s}^{-1}$ (●), $\dot{\gamma}=18\ \mathrm{s}^{-1}$ (○), $\dot{\gamma}=70\ \mathrm{s}^{-1}$ (▲), $\dot{\gamma}=110\ \mathrm{s}^{-1}$ (▽), and $\dot{\gamma}=170\ \mathrm{s}^{-1}$ (+). The time $t_e$ standing for the emergence of the scattering ring in SALS corresponds to $t_c$, the time to reach the minimum of conductivity. Inset: variation of $t_e$ and $t_c$ as a function of $\dot{\gamma}$. The solid lines correspond to the best power laws fits: $t_e=\gamma_e\dot{\gamma}^{-1}$ and $t_c=\gamma_c\dot{\gamma}^{-1}$. Different symbols stands for the measurements made in SALS (□): $t_e=(6150\pm380)\,\dot{\gamma}^{-(1.02\pm0.02)}$, and conductivity (■): $t_e=(5590\pm335)\,\dot{\gamma}^{-(0.98\pm0.03)}$.

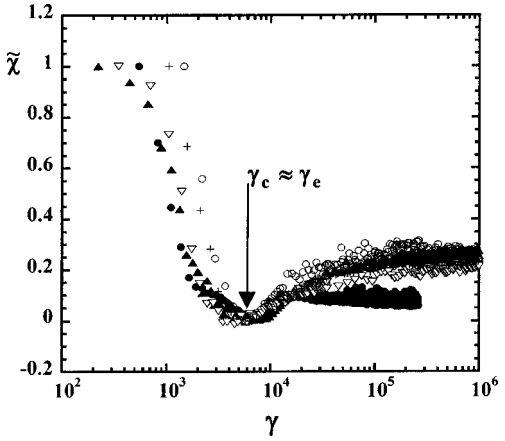


FIG. 26. Master curve: shown is the renormalized conductivity defined as $\tilde{\chi}=[(\chi(t)-\chi(t_e))/(\chi(0)-\chi(t_e))]$ vs the strain $\gamma=\dot{\gamma}t$. One finds experimentally $\gamma_e\approx\gamma_c\approx6000$.

domains, their size $R$, decreases, as for $L_\alpha$ systems, until elastic and viscous stresses balance each other (i.e., $R_M\propto\dot{\gamma}^{-1/2}$). Within this picture, the surface tension between $L_\alpha$ and $L_3$ phases does not play a significant part and, therefore, at this intermediate stage, the $L_3$ phase likely lies outside the $L_\alpha$ domains. Contrary to the behavior observed in $L_\alpha$ phases (onion textures), what can then explain the further increase of the droplet size? Indeed, once the droplets have reached this intermediate stage, the $L_3$ phase must intercalate between these droplets since we know that for $\dot{\gamma}\leqslant\dot{\gamma}_L$, the steady state droplets are immersed in the $L_3$ phase. Indeed, such a scenario (see Fig. 24) seems consistent with our kinetics observations. The increase of the droplet size at large time becomes slower as $\dot{\gamma}$ increases. This trend can be qualitatively understood if one recall that the $L_3$ phase must then invade a porous medium made of smaller pores (i.e., typically the minimum droplet size, $R_M$). When we perform conductivity measurements cell along the velocity direction (Fig. 25) once a constant shear rate is applied to the $L_\alpha/L_3$ mixture, two distinct regimes can also be distinguished. First, the conductivity decreases and after a time $t_c$ reaches a minimum; then it increases up to its steady state value. The variation of $t_c$ with $\dot{\gamma}$ shows that the conductivity presents a minimum once a constant critical strain $\gamma_c$ is reached (see the insets of Figs. 25 and 26). The value of this critical strain which is identical to that required for the emergence of the scattering ring in SALS (i.e., for the formation of initial multilamellar droplets) confirms that the *strain* is the *key parameter* to understand the formation of MLVs in $L_\alpha/L_3$ two-phase mixtures. As for onion textures obtained upon shearing $L_\alpha$ phases, the formation of multilamellar droplets in $L_\alpha/L_3$ phase-separated mixtures also seems to be triggered by a primary buckling instability of the membranes.

## CONCLUSION

Glassy assemblies made of closed compact multilamellar vesicles can be formed upon shearing both $L_\alpha$ phases (onion textures) and $L_\alpha/L_3$ phase-separated mixtures. In both systems, the vesicles are monodisperse and their steady state size can be tuned continuously from a few micrometers down to a tenth of it by merely changing the value of applied shear rate. For $L_\alpha$ phases, the vesicle volume fraction is always 100% whereas for $L_\alpha/L_3$ mixtures, it can be tuned from 0 to 100%. As a consequence, the physical mechanism controlling the steady state size is different in both cases. Thus, for $L_\alpha/L_3$ mixtures, the vesicle size ($R\propto\dot{\gamma}^{-1}$) results from a balance between capillary and viscous forces (''Taylor's droplets''), whereas for $L_\alpha$ phases, its variation with shear rate ($R\propto\dot{\gamma}^{-1/2}$) is still not yet understood. However, we have shown that in both cases the formation of vesicles occurs homogeneously in the shear cell at a fixed wave vector $q_e$, similar to what is expected for a hydrodynamic instability. For both systems, the variation of $q_e$ with experimental parameters (i.e., shear rate, smectic distance, and the gap spacing of the Couette cell) bears striking similarities with the theoretical predictions of Zilman and Granek [45]. These results strongly suggest that the formation of multilamellar vesicles is monitored by an instability of the lamellae under flow, as expected by recent theories. However, the existence of a large critical strain necessary to develop this instability is very mysterious. We hope that these still open questions will motivate theoretical works.

## ACKNOWLEDGMENTS

It is a pleasure to thank A. Colin, F. Nallet, and D. Roux for fruitful discussions, and T. Douar and M. Winckert for technical assistance. Part of this work was supported by University Bordeaux I (BQR 2001) and by the Conseil Régional d'Aquitaine (CTP Grant No. 980209202).

[1] See, for instance, *Micelles, Menbranes, Microemulsions and Monolayers*, edited by W. M. Gelbart, A. Ben-Shaul and D. Roux (Springer Verlag, New York, 1994).
[2] W. Helfrisch, Z. Naturforsch. Teil A **28a**, 693 (1973).
[3] See for instance, *Statistical Mechanics of Membranes and Surfaces*, edited by D. R. Nelson, T. Piran and S. Weinberg (World Scientific, Singapore, 1989).
[4] G. Porte, J. Phys. (Paris) **4**, 8649 (1992).
[5] R. G. Larson, *The Structure and Rheology of Complex Fluids* (Oxford University Press, Oxford, 1999), and references therein.
[6] O. Diat and D. Roux, J. Phys. II **3**, 9 (1993).
[7] J. Bergenholtz and N. J. Wagner, Langmuir **12**, 3122 (1996).
[8] A. Léon, D. Bonn, J. Meunier, A. Al-Kahwaji, O. Greffier, and H. Kellay, Phys. Rev. Lett. **84**, 1335 (2000).
[9] J. Zipfel, J. Berghausen, P. Lindner, and W. Richtering, J. Phys. Chem. B **103**, 2841 (1999).
[10] O. Dhez, F. Nallet, and O. Diat, Europhys. Lett. **55**, 821 (2001).
[11] G. Cristobal, A. Colin, J. Rouch, and P. Panizza, Phys. Rev. E **62**, 3871 (2000); **64**, 011505 (2001).
[12] L. Courbin, G. Cristobal, J. Rouch, and P. Panizza, Europhys. Lett. **55**, 880 (2001). Note that R in this reference stands for the vesicle radius.
[13] F. Gauffre and D. Roux, Langmuir **15**, 3738 (1999).
[14] D. W. Kim, S-G. Oh, S-C. Yi, S-Y. Bae, and S-K. Moon, Chem. Mater. **12**, 996 (2000).
[15] L. Courbin, J. Rouch, J. P. Delville, and P. Panizza, Phys. Rev. Lett. **89**, 148305 (2002).
[16] W. Helfrisch, Z. Naturforsch. Teil A **33a**, 305 (1978).
[17] O. Gosh and C. A. Miller, J. Phys. Chem. **91**, 4528 (1987).
[18] E. Freyssingeas, F. Nallet, and D. Roux, Langmuir **12**, 6028 (1996).
[19] D. Roux and A. M. Bellocq, Phys. Rev. Lett. **52**, 1895 (1984).
[20] E. Freyssingeas, Ph.D. thesis, Université de Bordeaux I, 1994.
[21] See for instance, R. S. Brodkey, *The Phenomena of Fluid Motion* (Dover, New York, 1967).
[22] L. Soubiran, C. Coulon, P. Sierro, and D. Roux, Europhys. Lett. **31**, 243 (1995).
[23] J. I. Escalante and H. Hoffmann, J. Phys.: Condens. Matter **12**, 438 (2000).
[24] O. Diat, F. Nallet, and D. Roux, J. Phys. II **3**, 1427 (1993).
[25] R. Weigel, J. Lauger, W. Richtering, and P. Lindner, J. Phys. II **6**, 529 (1996).
[26] T. D. Le, U. Olsson, and K. Mortensen, Langmuir **17**, 999 (2000); Phys. Chem. Chem. Phys. 1310 (2001); Physica B **276**, 379 (2000).
[27] For a recent review on the effect of shear on lamellar phases see K. Mortensen, Curr. Opin. Colloid Interface Sci. **6**, 140 (2001).
[28] T. Gulik-Krzywicki, J. C. Dedieu, D. Roux, C. Degert, and R. Laversanne, Langmuir **12**, 4668 (1996).
[29] P. Panizza, V. Vuillaume, D. Roux, C. Y. Lu, and M. E. Cates, Langmuir **12**, 248 (1996).
[30] S. Müller, C. Börschig, W. Gronski, C. Schmidt, and D. Roux, Langmuir **15**, 7558 (1999).
[31] O. Robles-Vasquez, S. Corona-Galvan, J. F. A. Soltero, and J. E. Puig, J. Colloid Interface Sci. **160**, 65 (1993).
[32] D. Roux, F. Nallet, and O. Diat, Europhys. Lett. **24**, 53 (1993).
[33] C. Meyer, S. Asnascios, C. Bourgaux, and M. Kleman, Mol. Cryst. Liq. Cryst. **332**, 531 (1999).
[34] C. Meyer, S. Asnascios, C. Bourgaux, and M. Kleman, Rheol. Acta **39**, 223 (2000).
[35] J. P. Poirier, *Creep of Crystals High Temperature: Deformation Processes in Metals, Ceramics and Minerals* (Cambridge University Press, Cambridge, 1985).
[36] G. I. Taylor, Proc. R. Soc. London, Ser. A **146**, 501 (1934).
[37] E. Van der Linden, W. T. Hogervorst, and H. N. W. Lekkerkerker, Langmuir **12**, 3127 (1996).
[38] E. Van Der Linden and J. H. Droge, Physica A **193**, 439 (1993).
[39] J. Zipfel, F. Nettesheim, P. Lindner, T. D. Le, U. Olsson, and W. Richtering, Europhys. Lett. **53**, 335 (2001).
[40] A. Léon, D. Bonn, J. Meunier, A. Al-Kahwaji, O. Greffier, and H. Kellay, Phys. Rev. Lett. **84**, 1335 (2000).
[41] F. Nettesheim, J. Zipfel, U. Olsson, F. Renth, P. Lindner, and W. Richtering, Langmuir **19**, 3603 (2003).
[42] P. Ostwald and M. Kléman, J. Phys. (France) Lett. **43**, L-411 (1983).
[43] P. Ostwald and S. I. Ben-Abraham, J. Phys. (Paris) **43**, 1193 (1982).
[44] A. S. Wunenburger, A. Colin, T. Colin, and D. Roux, Eur. Phys. J. E **2**, 277 (2000).
[45] A. G. Zilman and R. Granek, Eur. Phys. J. B **11**, 593 (1999).
[46] S. Marlow and P. Olmsted, Eur. Phys. J. E **8**, 485 (2002).
[47] J. Yamamoto and H. Tanaka, Phys. Rev. Lett. **74**, 932 (1995).
[48] P. Panizza, L. Soubiran, C. Coulon, and D. Roux, Phys. Rev. E **64**, 021502 (2001).
[49] M. E. Cates and S. T. Milner, Phys. Rev. Lett. **62**, 1856 (1989).
[50] L. Courbin and P. Panizza (unpublished).
[51] H. F. Majhoub, C. Bourgaux, P. Sergot, and M. Kleman, Phys. Rev. Lett. **81**, 2076 (1998).
[52] O. D. Lavrentovich, C. Quillet, and M. Kleman, J. Phys. Chem. B **101**, 420 (1997).
[53] B. J. Ackerson and N. A. Clark, Phys. Rev. A **30**, 906 (1984).
[54] O. Diat, D. Roux, and F. Nallet, Phys. Rev. E **51**, 3296 (1995).
[55] P. Sierro and D. Roux, Phys. Rev. Lett. **78**, 1496 (1997). See also: P. Sierro, Ph.D. thesis, Université Bordeaux I, 1995.
[56] T. G. Mason and J. Bibette, Langmuir **13**, 4600 (1997).